NUMERICAL SIMULATION OF HYDROGEN DEFLAGRATION USING CFD

PRATAP SATHIAH [1] AND ARUN K. AMPI

E-mail: *pratap.sathiah@shell.com*

[1] *Shell Technology Centre Bangalore, Shell India Markets Private Limited, Plot No - 7, Bangalore Hardware Park, Devanahalli, Mahadeva Kodigehalli, Bangalore - 562 149,*

Abstract

Hydrogen is seen as an important future energy carrier as part of the move away from traditional hydrocarbon sources. Delayed ignition of a hydrogen-air mixture formed from an accidental release of hydrogen in either a confined or congested environment can lead to the generation of overpressure impacting both people and assets. An understanding of the possible overpressures generated is critical in designing facilities and effective mitigation systems against hydrogen explosion hazards. This paper describes the numerical modelling of hydrogen deflagrations using a new application PDRFOAM-R that is part of the wider OpenFOAM open-source CFD package of routines for the solution of systems of partial differential equations. The PDRFOAM-R code solves momentum and continuity equations, the combustion model is based on flame area transport and the turbulent burning velocity correlation is based on Markstein and Karlovitz numbers. PDRFOAM-R is derived from publicly available PDRFOAM tool and it resolves small and large obstacles, unlike PDRFOAM which is based on the Porosity Distributed Resistance approach. The PDRFOAM-R code is validated against various unconfined-uncongested and semiconfined-congested explosion experiments. The flame dynamics and pressure history predicted from the simulation show a reasonable comparison with the experiments.

1 Introduction

Hydrogen is seen as an important future energy carrier as part of the move away from traditional hydrocarbon sources. Hydrogen is mainly produced through the electrolysis of water and the Steam Methane Reforming process. For the safer design of hydrogen production facilities, it is essential to understand the consequences that could arise following an accidental release of hydrogen, such as a jet fire or vapour cloud explosion. Explosions can be sub-classified depending on whether the explosion is within a confined or congested environment. The degree of confinement and/or congestion are the major parameters that influence the amount of pressure rise during a vapour cloud explosion of a hydrogen-air mixture.

When a flammable mixture, present in a congested environment is ignited, the unburnt gases ahead of the flame are pushed outwards by the burnt gases. Turbulence is generated when the unburnt gases flow through the congestion leading to an increase in the turbulent flame speed. In turn, this increase in flame speed leads to further increases in turbulence and flame speed, which ultimately generates overpressure. This positive feedback loop between turbulence and flame speed is known as the Schelkin mechanism.

In the case of an explosion in a confined geometry, the overpressure increases because of the compression of unburnt gases when it is pushed against confinement. In addition, this compression increases the pressure and temperature of the unburnt gases leading to an increase in turbulent flame speed which in turn increases the overpressure.

Either empirical or CFD based models can be used to estimate the overpressure resulting from vapour cloud explosions. TNO multi-energy method [1-2], TNT equivalency model [2-4], Baker-Strehlow method [2,5] and CAM [6] are the most commonly used empirical models. Each model has its simplification and assumptions which eventually limit the model to be used as a predictive tool outside the range of its validation. In order to overcome the issues associated with the predictive capability of the empirical models, more accurate CFD based numerical models are developed that take into account the interaction between the geometry and gas flow in a detailed manner to better predict flame propagation and pressure build-up. These codes are divided into codes using Porosity Distributed Resistance (PDR) approach [7] and CFD based approach. In a PDR based approach small-scale obstacles to be treated as sub-grid elements in the form of porosity and resistance elements, while large obstacles are resolved. This approach is used in the existing tools (commercial tools e.g. FLACS [8], EXSIM [9] and PDRFOAM[10]). There are other tools, which apply the PDR concept for explosion modelling e.g. in-house tool McNEWT [11] (developed in Cambridge University, United Kingdom) and COBRA [12]. The PDR concept has also been used in large scale fire modelling (for example in the commercially available KFX tool [13]). There are codes which use CFD based approach (e.g., ANSYS FLUENT, STARCCM+) which tend to resolve various obstacle (small and large). Here, a new CFD tool PDRFOAM-R is presented to predict the flame and pressure dynamics during the deflagration of a hydrogen-air mixture and validated against hydrogen explosion experiments available in the open literature. PDRFOAM-R is derived from a publicly available PDRFOAM tool developed within the wider OpenFOAM open-source CFD environment [14] which resolves small- and large-scale obstacles.

2 Numerical Methodology

The equations for mass, momentum, enthalpy and regress variables representing combustion progress are solved. The unsteady Favre-averaged (density-weighted) Navier-Stokes equations are solved along with the standard *k*-*ε* turbulence model. Also, the transport equations for the flame wrinkling parameter are solved. It is worth mentioning, that small and large obstacle is completely resolved instead of using porosity distributed resistance approach (used in PDRFOAM).

2.1 Governing Equations

The governing equations for mass, momentum and energy are as follows:

$$\frac{\partial}{\partial t}(\bar{\rho}) + \frac{\partial}{\partial x_i}(\bar{\rho}\widetilde{u_i}) = 0 \tag{1}$$

$$\frac{\partial}{\partial t}(\bar{\rho}\widetilde{u_i}) + \frac{\partial}{\partial x_j}(\bar{\rho}\widetilde{u_j}\widetilde{u_i}) = -\frac{\partial \bar{p}}{\partial x_i} + \bar{\rho}g_i + \frac{\partial}{\partial x_j}(\tau_{ij}) - \frac{\partial}{\partial x_j}\left(\bar{\rho}\widetilde{u_j''u_i''}\right) \tag{2}$$

$$\frac{\partial}{\partial t}(\bar{\rho}\tilde{h}) + \frac{\partial}{\partial x_j}(\bar{\rho}\widetilde{u_j}\tilde{h}) = \frac{\partial}{\partial x_j}\left(D_{h,L}\frac{\partial \tilde{h}}{\partial x_j}\right) - \frac{\partial}{\partial x_j}\left(\bar{\rho}\widetilde{u_j''h''}\right) + \left[\frac{\partial \bar{p}}{\partial t} - \frac{\partial \bar{\rho}\tilde{K}}{\partial t} - \frac{\partial\, \bar{\rho}\widetilde{u_j}\tilde{K}}{\partial x_j}\right] \tag{3}$$

$$\frac{\partial}{\partial t}(\bar{\rho}\widetilde{h_u}) + \frac{\partial}{\partial x_j}(\bar{\rho}\widetilde{u_j}\widetilde{h_u}) = \frac{\partial}{\partial x_j}\left(D_{hu,L}\frac{\partial \widetilde{h_u}}{\partial x_j}\right) - \frac{\partial}{\partial x_j}\left(\bar{\rho}\widetilde{u_j''h_u''}\right) + \frac{\bar{\rho}}{\rho_u}\left[\frac{\partial \bar{p}}{\partial t} - \frac{\partial \bar{\rho}\tilde{K}}{\partial t} - \frac{\partial\, \bar{\rho}\widetilde{u_j}\tilde{K}}{\partial x_j}\right]. \tag{4}$$

Here $\bar{\rho}$ and $\bar{p}$ are the Reynolds-averaged density and pressure, $\widetilde{u_i}$ is the Favre-averaged velocity, $\left(\bar{\rho}\widetilde{u_j''u_i''}\right)$ is the Reynolds stress tensor, which is closed using the isotropic eddy viscosity formulation as follows:

$$\bar{\rho}\widetilde{u_j''u_i''} = \mu_t\left(\frac{\partial \widetilde{u_i}}{\partial x_j} + \frac{\partial \widetilde{u_j}}{\partial x_i} - \frac{2}{3}\delta_{ij}\frac{\partial \widetilde{u_k}}{\partial x_k}\right) + \frac{2}{3}\bar{\rho}\tilde{k} \tag{5}$$

Here, the turbulent viscosity, μ_t, is given by

$$\mu_t = c_\mu \frac{\tilde{k}^2}{\tilde{\varepsilon}} \tag{6}$$

The SST *k-ω* turbulence model is used to calculate the turbulent kinetic energy, $\tilde{k}$, and specific turbulent dissipation rate, $\widetilde{\omega}$, which is governed by the following equations described in the next section:

2.2 Turbulence Model

The following shear stress transport (SST) equations of turbulent kinetic energy, $\tilde{k}$, and specific turbulent dissipation rate, $\widetilde{\omega}$, are solved

$$\frac{\partial}{\partial t}(\bar{\rho}\tilde{k}) + \frac{\partial}{\partial x_j}(\bar{\rho}\widetilde{u_j}\tilde{k}) = \frac{\partial}{\partial x_j}\left[\left(\mu + \frac{\mu_t}{\sigma_k}\right)\frac{\partial \tilde{k}}{\partial x_j}\right] + P - \bar{\rho}\widetilde{\omega} \tag{7}$$

$$\frac{\partial}{\partial t}(\bar{\rho}\widetilde{\omega}) + \frac{\partial}{\partial x_j}(\bar{\rho}\widetilde{u_j}\widetilde{\omega}) = \frac{\partial}{\partial x_j}\left[\left(\mu + \frac{\mu_t}{\sigma_\omega}\right)\frac{\partial \widetilde{\omega}}{\partial x_j}\right] + \alpha\frac{\widetilde{\omega}}{\tilde{k}}P - \bar{\rho}\,\widetilde{\omega}^2 + \sigma_d\frac{\bar{\rho}}{\widetilde{\omega}}\frac{\partial \widetilde{\omega}}{\partial x_j}\frac{\partial \tilde{k}}{\partial x_j} \tag{8}$$

where, *P,* is the source term relating to turbulence kinetic energy production due to the mean flow, which is given by:

$$P = \bar{\rho}\widetilde{u_j^{"}u_i^{"}}\frac{\partial \widetilde{u_i}}{\partial x_j}. \tag{9}$$

2.3 Combustion Model

A laminar flamelet approach is used for combustion modelling. This approach assumes that the flame is a thin interface that separates unburnt and burnt gases. In other words, the laminar flamelets are assumed to be much thinner than all the turbulent eddies and the probability of finding the reacting gas is very low compared to the probability of finding unburnt and burnt gas mixtures. The combustion progress in this approach is then described in terms of the progress variable *c,* (or regress variable, *b*) which is defined as follows:

$$c = (1 - b) = \frac{T - T_u}{T_b - T_u} = \frac{\rho - \rho_u}{\rho_b - \rho_u}. \tag{10}$$

T_b and T_u are the burnt and unburnt gas temperature, while ρ_u and ρ_b are the unburnt and burnt gas density. $b = 0$ $(c = 1)$ correspond to the combustion products, and $b = 1$ $(c = 0)$ corresponding to the unburnt fuel-air mixture. The governing equation for the Favre-averaged regress variable, $\tilde{b}$, is:

$$\frac{\partial}{\partial t}(\bar{\rho}\tilde{b}) + \frac{\partial}{\partial x_j}(\bar{\rho}\widetilde{u_j}\tilde{b}) = \frac{\partial}{\partial x_j}\left(D_L\frac{\partial \tilde{b}}{\partial x_j}\right) + \frac{\partial}{\partial x_j}\left(\bar{\rho}\widetilde{u_j^{"}b^{"}}\right) + \rho_u S_l\,\tilde{\Xi}\,|\Delta b| + \rho_u S_I \tag{11}$$

where the first term on the RHS is the contribution from laminar diffusion, the second term is the contribution from the turbulent flux which needs closure, the third term is the source term for the regress variable due to combustion and the final term is the contribution from the initial ignition.

The turbulent flux for the regress variable is closed using a classical gradient assumption as follows:

$$\widetilde{\bar{\rho}u_j''b''} = -\frac{\mu_t}{Sc_t}\frac{\partial}{\partial x_j}(\tilde{b}) = -D_t\frac{\partial}{\partial x_j}(\tilde{b}). \quad (12)$$

Here, D_t is the turbulent diffusion coefficient and D_L is the laminar diffusion coefficient in Equation (10). S_l in Equation (10) is the source term (the contribution from ignition) in the computational cells where ignition takes place. The source term is assumed to be proportional to ignition strength divided by ignition duration, which determines how fast the unburnt gas in that computational cell is converted to the burnt gas. If this ratio is too low, heat can diffuse away and the ignition is not sustained.

The source term for regress variable is based on a flame wrinkling factor, $\tilde{\Xi}$, which is defined as the ratio of the average of flame surface area per unit volume to that of the average flame area projected onto the mean direction of propagation per unit volume. This can be interpreted as the ratio of turbulent burning velocity S_t to laminar burning velocity S_l, when it reaches equilibrium and is given by:

$$S_t = S_l\tilde{\Xi} \quad (13)$$

Here, $\tilde{\Xi}$ is the flame wrinkling due to turbulence.

2.3.1 Flame Wrinkling Due to Turbulence

The governing equation for the $\tilde{\Xi}$ is given by:

$$\frac{\partial}{\partial t}(\bar{\rho}\tilde{\Xi}) + \frac{\partial}{\partial x_j}(\bar{\rho}\tilde{u_j}\tilde{\Xi}) = \phi_{Xi}|\nabla\tilde{\Xi}| + \bar{\rho}G\tilde{\Xi} - \bar{\rho}R(\tilde{\Xi} - 1) \quad (14)$$

The flux (ϕ_{Xi}) for the $\tilde{\Xi}$ maybe written as:

$$\phi_{Xi} = \rho_u S_t\overrightarrow{n_f} + \bar{\rho}S_l\left(\frac{1}{\tilde{\Xi}} - \tilde{\Xi}\right)\overrightarrow{n_f} - \frac{\frac{\partial}{\partial x_j}\left(D_{eff}\frac{\partial\tilde{b}}{\partial x_j}\right)}{|\nabla\tilde{b}|}\overrightarrow{n_f} \quad (15)$$

Where, $\overrightarrow{n_f}$ is the vector normal to the face and D_{eff} is the effective diffusivity, which is defined as the summation of laminar and turbulent diffusivity. G and R are the rate coefficient for the generation term and removal rate.

$$G = R\frac{\Xi_{eq}-1}{\Xi_{eq}} \quad (16)$$

where

$$\Xi_{eq\theta} = 1 + \left[1 + 2\Xi_{coef}(0.5 - \tilde{b})\right](\Xi_{eq*} - 1) \quad (17)$$

Here,

$$\Xi_{eq*} = \frac{R}{R - G_\theta}, \quad (17)$$

where

$$R = G_\theta \frac{\Xi_{eq\theta}}{\Xi_{eq\theta}-1}. \quad (18)$$

The total flame wrinkling $\Xi_{teq\theta}$ is the equilibrium value that Ξ would asymptote to if conditions do not change over a sufficiently long distance and are given by

$$\Xi_{eq\theta} = \Xi_{eqturb.} = \frac{S_t}{S_l} \quad (19)$$

Ξ_{eqturb} is the wrinkling contribution due to turbulence and it is described in Subsection 2.3.2.

2.3.2 Turbulent Burning Velocity

For the case of mild turbulence and laminar instability (i.e. the case of Karlovitz number less than 0.1), the turbulent burning velocity correlation by Gulder [15] in the regime of low turbulence is given by

$$S_t = 0.62 \left(\frac{u''}{S_l}\right)^{0.5} R_l^{0.25} \quad (20)$$

Where R_l is the turbulent Reynolds number. Equation (20) may be rewritten in terms of Karlovitz number as follows:

$$S_t = 0.31 \left(\frac{u''}{S_l}\right)\left(\frac{u''}{KS_l}\right)^{0.5} \quad (21)$$

The correlations presented in Equation (20) is used for the estimation of Ξ_{eqturb} (see Equation (19)).

In addition to the above equations, energy equations are solved which is not described in detail.

2.4 Numerical Method

The equations sets are cast in conservative form and solved using a finite-volume approach. The solution numerical schemes are standard OpenFOAM solvers and schemes. OpenFOAM has the capability of real-time switching of the solvers and schemes depending upon the entries in the dictionary. The solver is switched based on the criterion of pressure values. Different Gaussian numerical schemes are used for gradient, divergence and Laplacian terms of the transport equation. An Euler scheme is used for the temporal term of the equation. A preconditioned conjugate or biconjugate gradient method is used for solving all the dependent variables with an absolute tolerance level of 10^{-9}. It is worth stressing that the PDRFOAM solver can be used in parallel therefore it essentially means that computational time.

3 Results and Discussion

The numerical solution procedure, the governing equations from, Eqs. (1)– (4), Eqs. (6)-(7) and Eqs. (10) are solved using the finite-volume technique and are treated employing the second-order discretization method. The pressure and velocity coupling of the momentum and mass conservation equations were handled using the PIMPLE algorithm, in conjunction with a *k*–ω SST model which is the combination of PISO (pressure-implicit split-operator) and SIMPLE algorithm. No-slip and adiabatic boundary conditions are imposed on the wall surfaces. Wave transmissive boundary condition is applied to the pressure, which

takes into account the non-reflective pressure conditions. The computational domain was discretized using an OpenFOAM utility called 'snappyHexMesh', which has the provision to capture the congested obstacle more accurately. It is worth mentioning that tuning of the model constants was not performed. A mesh size ranges from 2-50 mm depending on the case, overall mesh count is between ~ 1-6 million. Grid sensitivity studies are performed but not reported due to the limitation in number of pages.

3.1 Uncongested Vapour Cloud Explosion-Unconfined

Vapour cloud experiments by Sato et al. [16] were performed in a 5.6 m^3 and 37 m^3 rectangular domain. A plastic sheet was used to hold the quiescent homogenous hydrogen-air mixture and ignition is provided at the centre of the domain at ground level. Ionization probes and pressure transducers were used to measure the flame front dynamics and overpressure. The experiment was performed with two different hydrogen concentrations of 20 and 30%. The schematic of the 5.6 m^3 and 37 m^3 experimental rigs are shown in Figure 1. It is to be noted that the flame arrival time was only measured for the stoichiometric condition (i.e. the hydrogen concentration of 30 %).

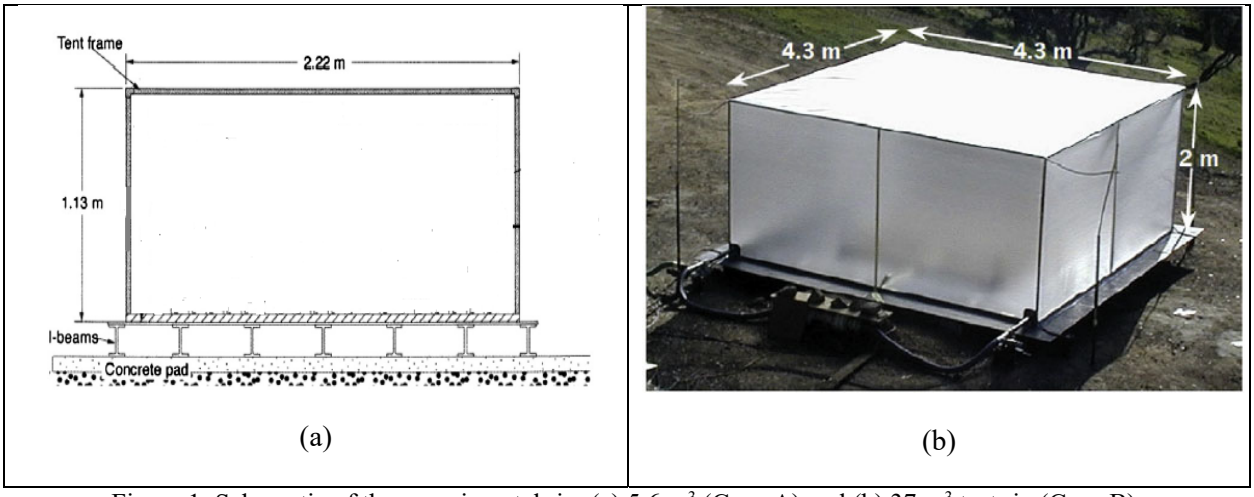

Figure 1: Schematic of the experimental rig; (a) 5.6 m^3 (Case-A) and (b) 37 m^3 test rig (Case-B).

Figure 2: Flame propagation (iso-surface of regress variable, *b*) at different times i.e., 15 ms, 25 ms, 35 ms, 45 ms and 55 ms, (left to right), respectively. The results correspond to Case-A (hydrogen concentration 30 %). The figure represents one-quarter of the box.

The flame propagation can be divided into four different phases; a) ignition, b) quasi-laminar flame propagation, c) slow deflagration and d) fast deflagration phase. Since there is no obstacle, only two phases can be observed, i.e., ignition and quasi laminar flame propagation phase. The flame and pressure dynamics predicted from the simulations are compared with the experiments. Figure 2 shows the iso-surface of regress variable, *b,* at different times, i.e., 15 ms, 25 ms, 35 ms, 45 ms and 55 ms, respectively. As the flame front propagates, the unburnt gas ahead of the flame is pushed outwards leading to an increase in turbulence which increases the turbulent flame speed. Figure 3 shows the comparison of flame arrival time as a function of distance for Case-A obtained using experiment and simulation. It can be seen that the turbulent flame speed is underpredicted in the simulation (~173 m/s) compared to the experiment (~217 m/s). This could be associated with a lack of modelling of the quasi-laminar flame propagation phase. This underprediction

leads to underprediction in the maximum overpressure (see Figure 4). All the simulation run has been performed with turbulence model as SST *k-ω*.

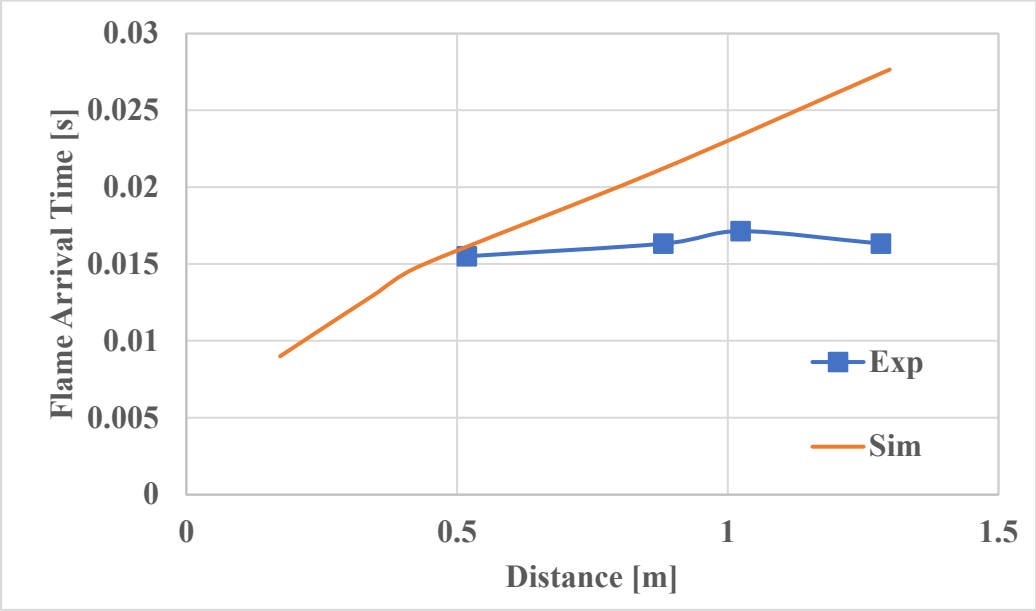

Figure 3: The variation of flame arrival time as a function of distance. The results correspond to a hydrogen concentration of 30 % (Case-A).

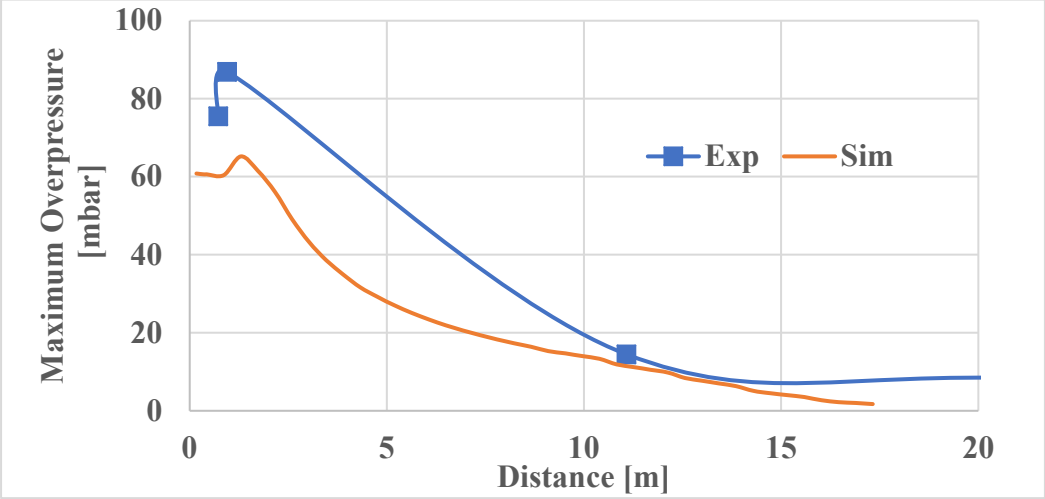

Figure 4: The variation of maximum overpressure as a function of distance. The results correspond to a hydrogen concentration of 30 % (Case-A).

Figure 5: Flame propagation (iso-surface of regress variable, *b*) at different times 15 ms, 25 ms, 35 ms, 45 ms and 55 ms (left to right). The results correspond to Case-B for stoichiometric hydrogen concentration. The figure represents one-quarter of the box.

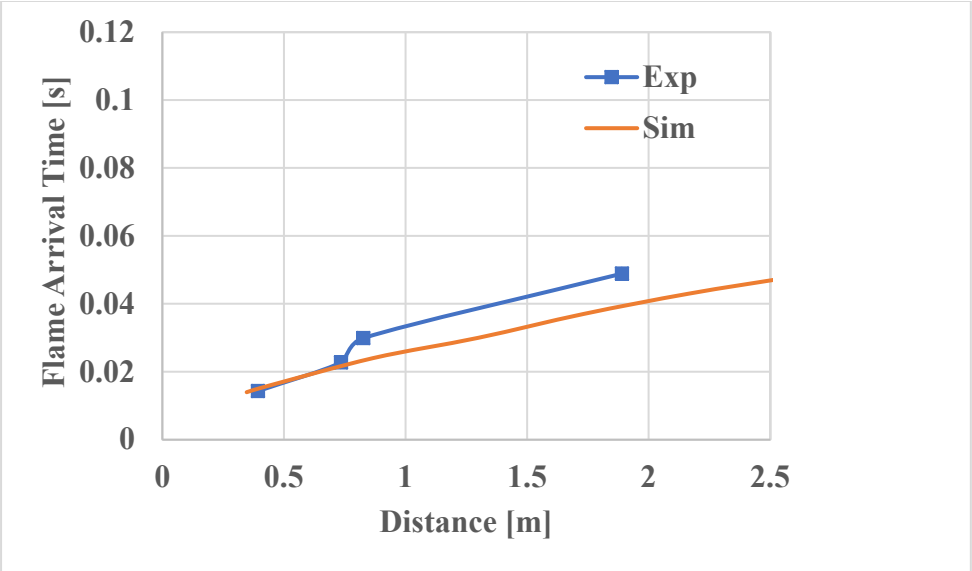

Figure 6:The variation of flame arrival as a function of distance. The results correspond to a hydrogen concentration of 30 % (Case-B).

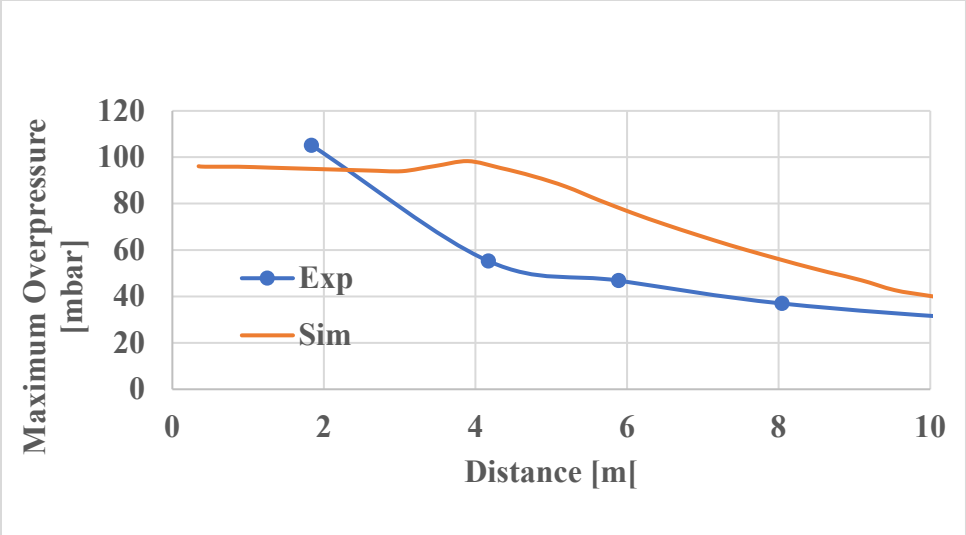

Figure 7: The variation of maximum overpressure as a function of distance. The results correspond to a hydrogen concentration of 30 % (Case-B).

Figure 5 shows the iso-surface of regress variable b at different times, i.e., 15 ms, 25 ms, 35 ms, 45 ms and 55 ms respectively. The flame propagation, in this case, is similar to the previous case (Case-A). i.e., the flame shape is spherical and the flame continues to accelerate as it moves away from the ignition location. Figure 6 shows the variation of the flame arrival as a function of distance obtained from the simulation and experiment for Case-B. Unlike Case-A, it can be noticed that the maximum turbulent flame speed is

overpredicted in simulation (~66 m/s) compared to the experiment (~45 m/s). This leads to overprediction in the maximum overpressure (see Figure 7) at distance greater than 2 m from the centre of the rig. It can be noticed that turbulent flame speed obtained using simulations show opposite trends, in one case is underpredicted and in the second case is overpredicted. Further work would be needed to understand the reason for over-prediction or underprediction. It could also be associated with the uncertainty of experiments.

3.2 Uncongested Vapour Cloud Explosion - Confined

Gas explosion experiment performed by Lv et al. [17] on a rectangular duct with a cross-section of 0.1 x 0.1 m^2 and a height of 0.5 m. The bottom end of the tube was closed by a steel plate. Figure 8 (a) shows the schematic of the vertical experimental rig. The top-end of the duct was covered with PVC membrane which ruptures at low pressure during the explosion. The stoichiometric hydrogen-air mixture introduced inside the duct and the ignition was provided at the centre of the duct at the ground level.

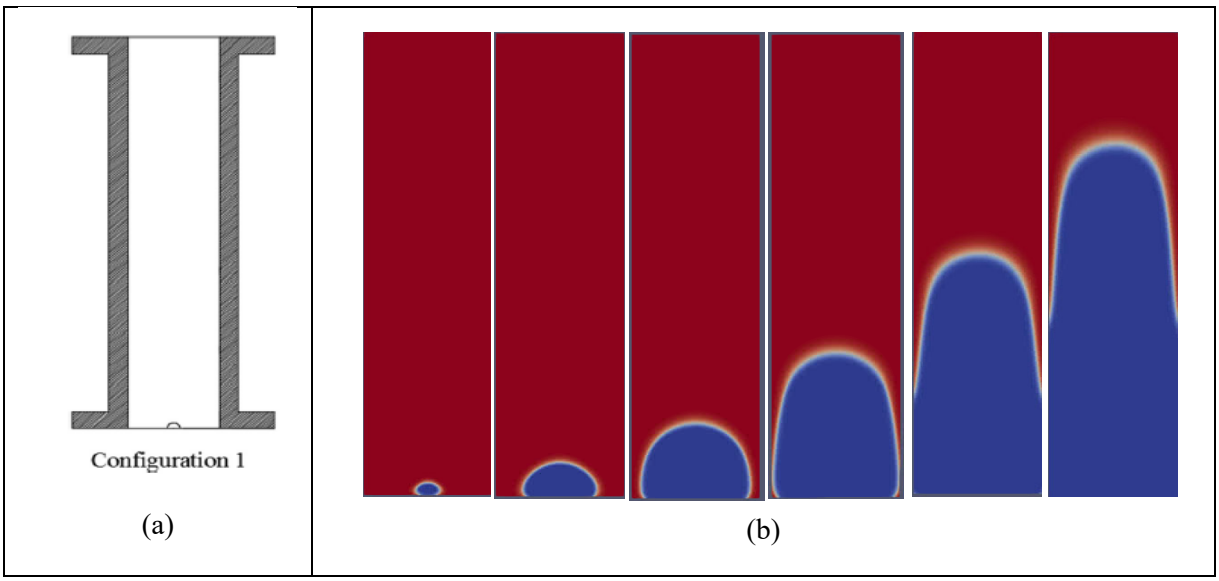

Figure 8: (a) Schematic of the 5 L experimental rig with no obstacle (Configuration 1) and (b) Flame propagation (iso-surface of regress variable, *b*) at different times 1 ms, 2 ms, 3 ms, 4 ms 5 ms and 6 ms (left to right) respectively.

Configuration 1 represents the experimental configuration without an obstacle, and it is shown schematically in Figure 8 (a). Figure 8 (b) shows the iso-surface of regress variable *b* at different times, i.e., 1 ms, 2 ms, 3 ms, 4 ms, 5 ms and 6 ms, respectively. It can be observed that the flame starts initially as spherical. After the ignition, the flame moves into the quasi-laminar flame propagation phase. During this phase the flame shape is spherical (growing in size between 1- 3 ms). At about 6 ms, the flame shape is elongated in a vertical direction because it comes in contact with the walls at the sides. The variation of flame arrival time as a function of distance obtained from the simulation is compared against the experiment (see Figure 9). The maximum turbulent flame speed (~183 m/s) is underpredicted in simulation when compared to the experiment (~259 m/s). This underprediction leads to underprediction in the maximum overpressure (see Figure 10) is due to the lack of quasi-laminar flame propagation phase.

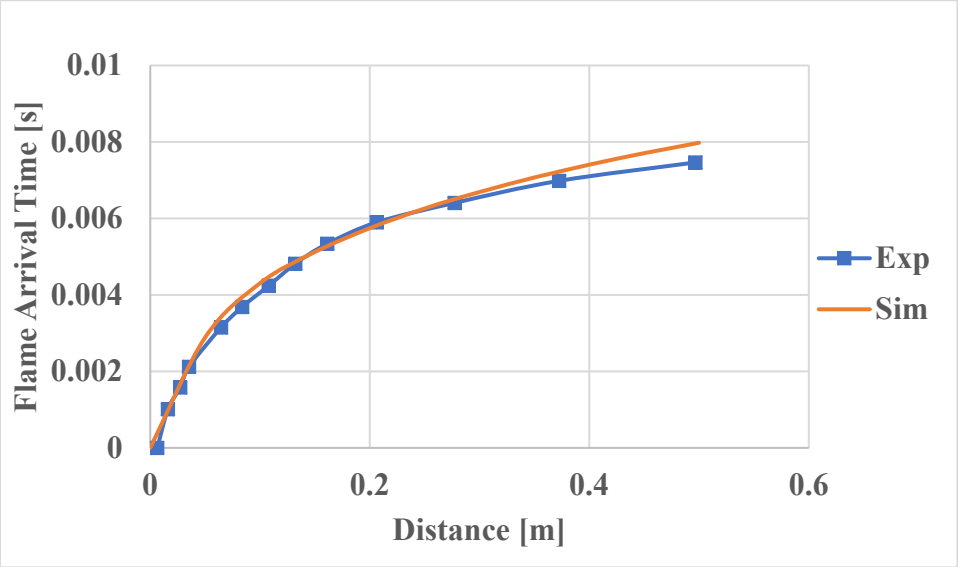

Figure 9: The variation of flame arrival time as a function of distance for Configuration 1.

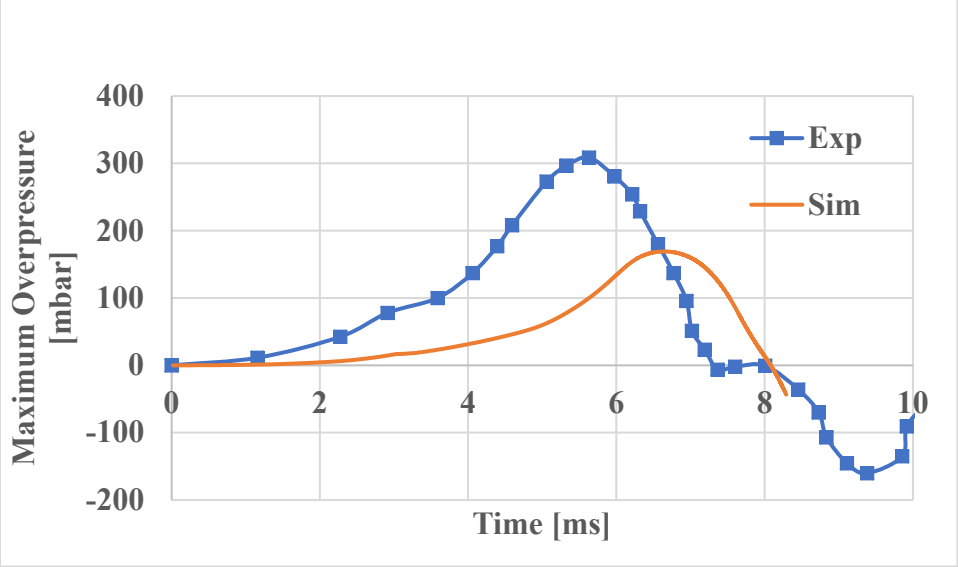

Figure 10: The variation of maximum overpressure as a function of time at a location of 0.15 m from the ignition point for Configuration 1.

3.3 Congested Vapour Cloud Explosion – Confined

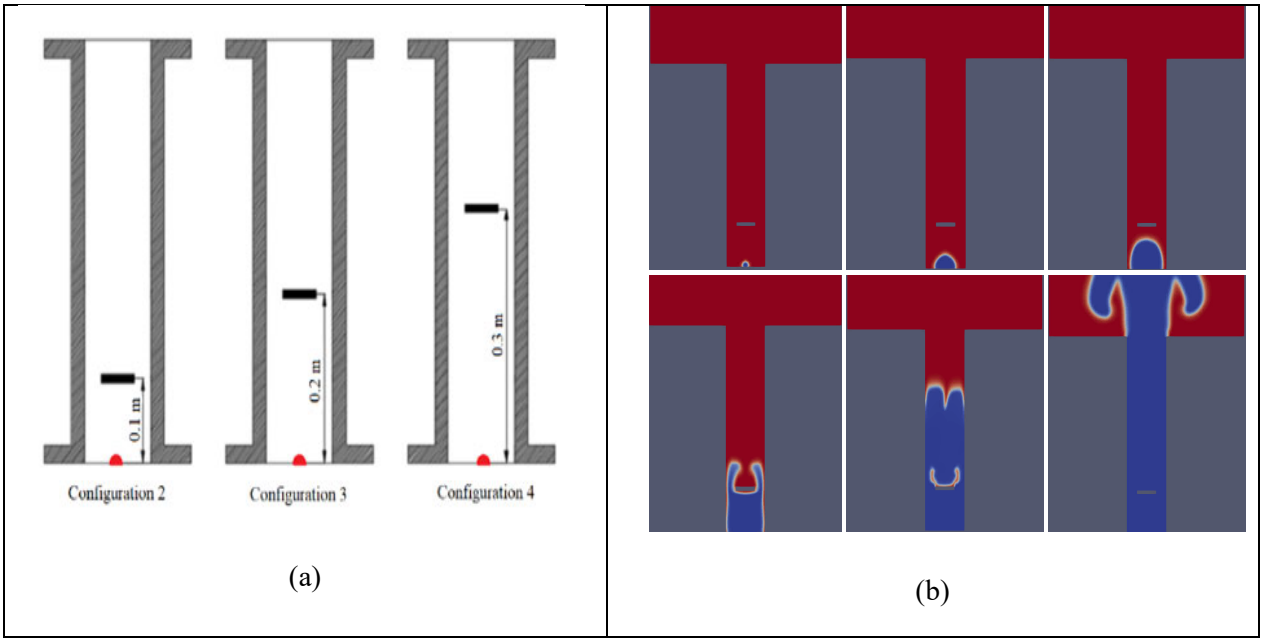

Figure 11: (a) Schematic of the experimental rig for three different configurations (Configuration 2-4) and (b) flame propagation at different (iso-surface of regress variable, *b*) times i.e., 1 ms, 2 ms, 3 ms, 4 ms, 5 ms and 6 ms, respectively. The results are shown for Configuration 2.

The explosion experiment was [18] performed on a rectangular duct with a cross-section of 0.1 x 0.1 m^2 and a height of 0.5 m and the bottom end of the tube was closed by a steel plate. An obstacle was located inside the duct that had a cross-section of 0.1 x 0.05 m^2 and a height of 0.01 m which gives a blockage ratio of 50 %. Three experimental configurations, with different obstacle locations, were used to analyse the impact of obstacle location on maximum explosion overpressure. A stoichiometric hydrogen-air mixture was introduced inside the duct. The schematic of the experimental configurations is shown in Figure 11 (a). Configurations 2 – 4 represent the experimental configurations with an obstacle located at 0.1 m, 0.2 m, and 0.3 m from the bottom end of the duct, respectively.

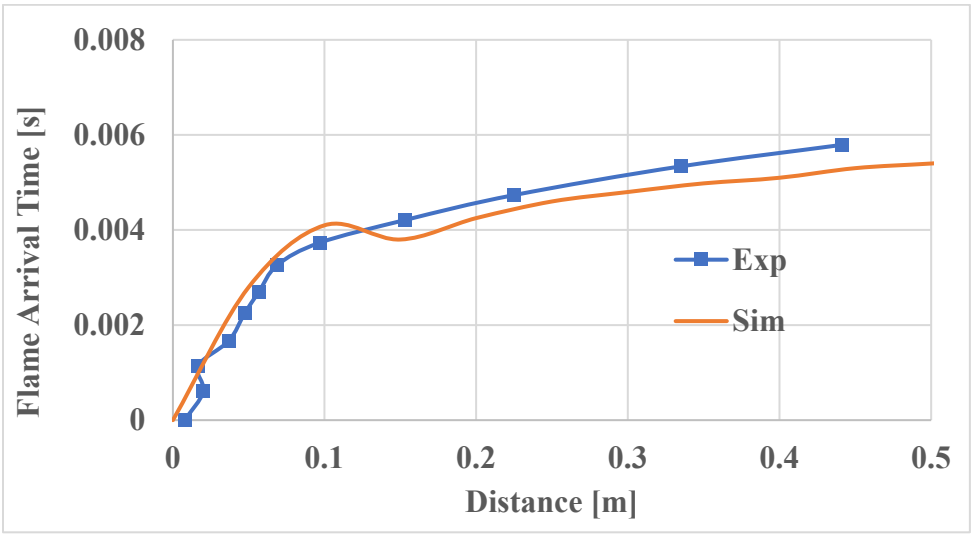

Figure 12: The variation of flame arrival time as a function of distance for Configuration 2.

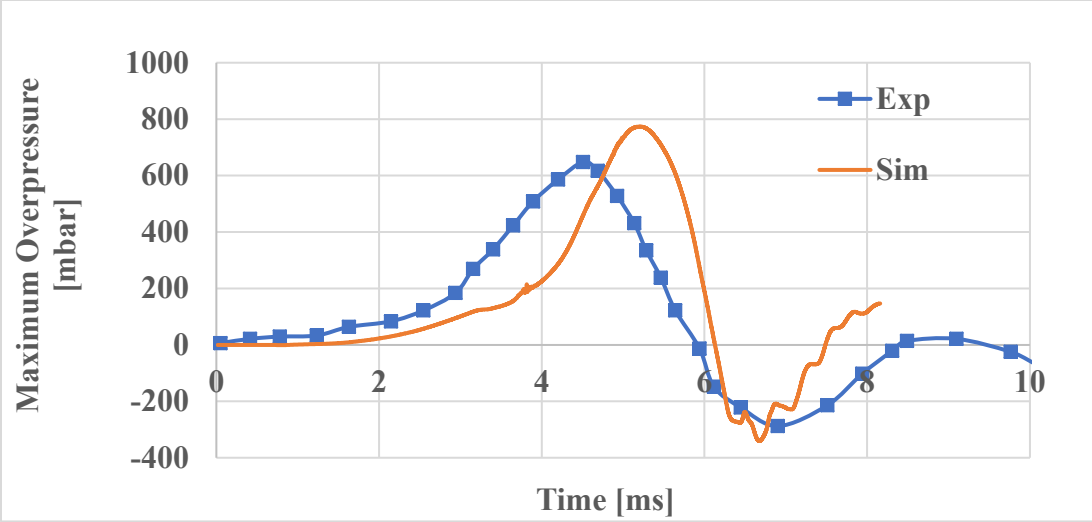

Figure 13: The variation of maximum overpressure as a function of time at a location of 0.15 m from the ignition point for Configuration 2.

The ignition was provided at the centre of the duct at the ground level. Figure 11 (b) shows the iso-surface of regress variable *b* at different times, i.e., 1 ms, 2 ms, 3 ms, 4 ms, 5 ms and 6 ms, respectively. It can be noticed that similar to configuration 1, the flame starts initially as hemispherical (1 - 3 ms). At a later stage, it becomes flat as it approaches the obstacle. Finally, towards the end, the flame exits the domain as mushroom-shaped. It is to be noted that similar behaviour of flame shape is observed in other configurations 3 and 4. In this case, four phases (ignition, quasi laminar and slow and fast deflagration phase) of flame propagation are observed. When compared to Configuration 1, the turbulent flame speed is high due to the presence of the obstacle. The flame interacts with obstacles leading to wrinkling of the flame which increases the turbulent flame speed. The increase in the turbulent flame speed leads to an increase in the maximum overpressure. Figure 12 shows the variation of flame arrival time as a function of distance. Figure 13 shows the time variation of maximum overpressure at the probe point. The simulation overpredicts the maximum overpressure when compared to experiments.

3.4 Quantitative Comparison

Table 1 shows the maximum overpressure predicted from the simulation and obtained from the experiments. From the table, it can be observed that the overpressure increases with an increase in the size of the domain and congestion.

Table 1: Comparison of maximum overpressure between experiment and simulation.

Serial Number	Type of domain	Case	Numerical prediction maximum overpressure (mbar)	Experimental maximum overpressure (mbar)	% Uncertainty
1	Unconfined and Uncongested	5.6 m^3 [16]	65.2	86.8	-24.9
			15.7	25.8	-39.2

2	Unconfined and Uncongested	37 m^3 [16]	95.1	105.1	-9.5
			20.7	19.1	+8.3
3	Unconfined and Uncongested	75 m^3 [18]	85	78.7	+8.0
4	Unconfined and Uncongested	200 m^3 [18]	128.7	114.8	+12.0
5	Unconfined and Uncongested	300 m^3 [19]	144.6	215.1	-32.78
6	Confined and Uncongested	C1 [17]	166.54	307.1	-45.7
7	Confined and Congested	C2 [17]	766.34	647.8	+18.3
8	Confined and Congested	C3 [17]	930.34	942	-1.2
9	Confined and Congested	C4 [17]	1268.1	905.3	+40.1

4 Conclusion and Future Work

PDRFOAM-R is derived from a publicly available PDRFOAM [10] tool developed within the wider OpenFOAM open-source CFD environment [14] which resolves small and large-scale obstacles. PDRFOAM-R was validated against uncongested and congested small scale experiments. The effect of an increase in the size of the domain, increase in hydrogen concentration, and presence of congestion was investigated. The flame arrival time and maximum overpressure with distance are compared against experiments. In most of the experiments, the flame arrival time and pressure decay are predicted well. However, there are few cases where the simulation is underpredicted. Further work is needed to understand the underprediction especially the inclusion of sub-model for the quasi-laminar flame propagation phase. More validations are undergoing to assess the predictive capability of PDRFOAM-R.

Reference

1. A. C. Van den Berg, The multi-energy method: a framework for vapour cloud explosion blast prediction. J. Hazard Mater. 12 (985), 1–10.
2. CCPS, Guidelines for Consequence Analysis of Chemical Release. Centre for Chemical Process Safety. AICHE, New York (1999).
3. W. Brasie, W. Simpson, Guidelines for estimating damage explosion. J. Loss. Prevent. Proc. 2, 91 (1968).

4. D. A. Decker, An Analytical Method for Estimating Overpressure from Theoretical Atmospheric Explosions. NFPA Annual Meeting. May. National Fire Protection Association, Quincy, MA, (1974).
5. Q. A. Baker, M. J. Tang, E. Scheier, G. J. Silva, Vapor cloud explosion analysis. In: AIChE 28th Loss Prevention Symposium, Atlanta, Georgia (1994), 1–31.
6. Congestion Assessment Method (CAM), FRED, Shell Global Solutions.
7. Hjertager, B. H., 1982. Numerical simulation of flame and pressure development in gas explosions. In SM Study no. 16, Univ. Waterloo Press, Ontario, Canada, pp. 407–426.
8. van Wingerden, K., Storvik, I., Arntzen, B. J., Teigland, R., Bakke, J. R., Sand, I. O., Sorheim, H. R., 1993. FLACS-93, a new explosion simulator. In 2nd. International Conference on Offshore Structural Design against Extreme Loads, London.
9. Hjertager, B. H., Saeter, O., Solberg, T., 1996. Numerical modelling of gas explosions - a review. 2nd Specialist Meeting on Fuel-Air Explosions, CMR, Bergen, Norway, June 26-28.
10. J. Puttock, F. Walter, D. Chakraborty, S. Raghunath and P. Sathiah, Numerical simulations of gas explosion using Porosity Distributed Resistance Approach Part -1: Validation against small-scale experiments, Submitted to International Journal.
11. Cant, R. S., 2007. Modelling and simulation of accidental combustion in complex geometries", In Proceedings of the 5th International Seminar on Fire and Explosion Hazards, Edinburgh, UK pp. 23–27.
12. Park, D. J. and Lee, Y. S., 2009, A comparison on predictive models of gas explosions, Korean J. Chem. Eng., 26(2), 313–323.
13. Magnussen, B.F., Lilleheie, N. I., Vembe, B.E., Lakså, B., Grimsmo, B., Lilleeng, L. A., Kleiveland, R., Rian, K. E., Olsen, R., Evanger, T., 2010. Numerical Computation of Large Scale Fires and Fire Mitigation – from Combustion Science to Industry Application. In Proceedings of the Sixth International Seminar on Fire and Explosion Hazards, University of Leeds, U.K, April 11-16.
14. OpenCFD Ltd. (2005). OpenFOAM (Opensource Field Operation And Manipulation).
15. Gulder, O. L. (1990). Turbulent premixed combustion modelling using fractal geometry. International Combustion Symposium., 23, 835–842.
16. Y. Sato, H. Iwabuchi, M. Groethe, E. Merilo, S. Chiba, Experiments on hydrogen deflagration, Journal of Power Sources 159 (2006) 144–148.
17. X. Lv, L. Zheng, Y. Zhang, M. Yu, Y. Su, Combined effects of obstacle position and equivalence ratio on overpressure of the premixed hydrogen-air explosion, International Journal of Hydrogen Energy 41 (2016) 17740-17749.
18. K. Wakabayashi, Y. Nakayama, T. Mogi, D. Kim, T. Abe, K. Ishikawa, E. Kuroda, T. Mastumura, S. Horiguchi, M. Oya, S. Fujiwara, Experimental study on blast wave generated by deflagration hydrogen-air mixture upto 200 m^3, Sci -Tech.Engineering Materials, 68 (2007).
19. M. Groethe, E. Merilo, J. Colton, S. Chiba,Y. Sato, H. Iwabuchi, Large-scale hydrogen deflagrations and detonations, International Journal of Hydrogen Energy 32 (2007) 2125 – 2133.